

Invariant regimes of Spencer scaling law for magnetic compression of rotating FRC plasma

Yiming Ma¹, Ping Zhu^{1,2*}, Bo Rao^{1*} and Haolong Li³

State Key Laboratory of Advanced Electromagnetic Technology, International Joint Research Laboratory of Magnetic Confinement Fusion and Plasma Physics, School of Electrical and Electronic Engineering, Huazhong University of Science and Technology, Wuhan, 430074, China

² Department of Nuclear Engineering and Engineering Physics, University of Wisconsin-Madison, Madison, Wisconsin 53706, USA

³ College of Physics and Optoelectronic Engineering, Shenzhen University, Shenzhen 518060, China

E-mail: zhup@hust.edu.cn, borao@hust.edu.cn

Abstract.

The scaling laws for the magnetic compression of a toroidally rotating field reversed configuration (FRC) have been investigated in this work. The magnetohydrodynamics (MHD) simulations of the magnetic compression on rotating FRCs employing the NIMROD code [C. R. Sovinec *et al.*, J. Comput. Phys. **195**, 355 (2004)], are compared with the Spencer's one-dimensional (1D) theory [R. L. Spencer *et al.*, Phys. Fluids **26**, 1564 (1983)] for a wide range of initial flow speeds and profiles. The toroidal flow can influence the scalings directly through the alteration of the compressional work as also evidenced in the 1D adiabatic model, and indirectly by reshaping the initial equilibrium. However, in comparison to the static initial FRC equilibrium cases, the pressure and the radius scalings remain invariant for the magnetic compression ratio B_{w2}/B_{w1} up to 6 in presence of the initial equilibrium flow, suggesting a broader applicable regime of the Spencer scaling law for FRC magnetic compression. The invariant scaling has been proven a natural consequence of the conservation of angular momentum of both fluid and magnetic field during the dynamic compression process.

Keywords: field reversed configuration, compact toroid, magnetic compression, MHD simulation, toroidal flow

1. Introduction

The field reversed configuration (FRC) is a high- β compact toroid primarily sustained by the poloidal magnetic field generated from plasma diamagnetic currents [1, 2]. As a promising candidate path to compact fusion, the FRC has the linear device geometry, the extended lifetime surpassing magnetohydrodynamics (MHD) expectations [3, 4, 5], and the capability to withstand highly dynamic processes such as supersonic translation and collision merging [6, 7, 8, 9, 10, 11, 12]. The magnetic compression over a short timescale

(tens of microseconds) has been demonstrated as an effective heating method for FRCs in experiments [13, 14, 15, 16]. The scaling predictions from the one-dimensional (1D) adiabatic compression model by Spencer [17] has been compared with FRX-C/LSM (Field-Reversed Experiment-C/Large ‘S’ Modification) experiments [15] and MHD simulations [18, 19]. Starting from static FRC equilibria in absence of any toroidal flow, previous simulation results [19] agree with the experiments [15] qualitatively while confirming some key scaling and geometry relations in the analytical model [17], despite the fact that in reality, FRCs often have strong toroidal rotation at the order of $0.1V_A$ [14, 20, 21, 22, 23, 24, 25]. The degree to which this agreement might be coincidental, the mechanisms by which toroidal flow may influence the scalings, and the potential existence of invariant scaling regimes in presence of flow all remain unclear.

In this work, we investigate these issues in a set of new simulations of the magnetic compression processes starting from initially rotating FRC equilibria using the resistive MHD model implemented in the NIMROD code [26, 27, 28]. The toroidal flow effects have been studied using a variety of steady equilibria characterized by various flow profiles and speeds as well as density profiles. The invariant regimes have been identified where the scalings for magnetic compression remain almost unchanged even for the initially rotating FRCs. It turns out that such an invariance of scaling originates from the conservation of angular momentum during the dynamic compression process.

The rest of paper is organized as follows. After a brief discussion on the 1D adiabatic model in section 2.1, the numerical approach and simulation results are described in section 3. Finally, the discussion and conclusions are presented in section 4.

2. Analytical model

2.1. 1D adiabatic compression model

A schematic plot of the FRC is shown as figure 1(a). For the highly elongated FRCs in absence of initial equilibrium flow, the quasi-static adiabatic compression yields $dW = dE$, where the dW is the external work done on the separatrix and dE is the increment of the total FRC energy $E = \int (p/(\gamma - 1) + B^2/(2\mu_0)) dV$. Considering the static equilibrium force balance

$$p_m = p(\psi) + \frac{B_z^2(\psi)}{2\mu_0} = \frac{B_w^2}{2\mu_0} \quad (1)$$

along with the field line structural relation $r_s = \sqrt{2}r_o$ and the axial force balance condition $\langle\beta\rangle = 1 - x_s^2/2$ [29, 30], the adiabatic compression scaling laws for both the magnetic and wall compressions can be obtained from the adiabatic relation $dW = dE$ [17, 31], where p_m is the maximum plasma pressure, B_w is the magnetic field outside the FRC plasma, r_s is the major radius of separatrix, r_o is the radius of the magnetic axis or O-point, $\langle\beta\rangle$ is the average plasma β over the middle plane within the separatrix, $x_s = r_s/r_w$ is the ratio of separatrix radius to the wall radius, ψ is the poloidal flux and the cylindrical coordinates (r, θ, z) is adopted. The Spencer scaling

laws for magnetic compression [17] are listed in table 1, where l is the length of the FRC, ϵ is a flux profile index, n_m is the maximum number density and T_m represents the maximum total plasma temperature. The $\epsilon = 0.25$ is adopted in this study in line with previous scaling law applications [32, 33].

Table 1. Spencer's scaling laws [17] for magnetic compression, $\epsilon > 0$ and $\gamma = 5/3$

parameter	scaling law
B_w	$x_s^{-(3+\epsilon)}$
p_m	$x_s^{-2(3+\epsilon)}$
l	$x_s^{\frac{2(4+3\epsilon)}{5}} \langle \beta \rangle^{\frac{-(3+2\epsilon)}{5}}$
n_m	$x_s^{\frac{-6(3+\epsilon)}{5}} \langle \beta \rangle^{\frac{-2(1-\epsilon)}{5}}$
T_m	$x_s^{\frac{-4(3+\epsilon)}{5}} \langle \beta \rangle^{\frac{2(1-\epsilon)}{5}}$

The flow effects can be preliminarily assessed within the adiabatic model and subsequently subjected to quantitative analysis through 2D MHD simulations. The force balance in the 1D steady FRC equilibrium is described by the equation

$$\frac{d}{dr} \left(p + \frac{B_z^2}{2\mu_0} \right) = \rho \Omega^2 r \quad (2)$$

where ρ is the mass density and Ω is the toroidal or azimuthal rotation frequency. Upon integrating equation (2) and assuming the rotation and density profiles from the rigid rotor (RR) model, equation (2) can be simplified as

$$p + \frac{B^2}{2\mu_0} = \frac{m_i n_m \Omega^2 r_s^2 \tanh(ku)}{4k} + p_m \quad (3)$$

with the relation $r_s = \sqrt{2}r_o$ and the condition $p(r = r_o) = p_m$. More specifically the rotation frequency $\Omega = u_\theta/r = \text{const}$ and

$$n = n_m \text{sech}^2(ku) \quad (4)$$

are adopted in the RR model, where k is the shape factor and the minor radius variable $u = 2r^2/r_s^2 - 1$. The total FRC energy $E = \int (p/(\gamma - 1) + B^2/(2\mu_0) + \rho \Omega^2 r^2/2) dV$ then can be written as

$$E = p_m V \left(1 + \frac{1}{2} \langle \beta \rangle \right) + \frac{1}{4} m_i n_m \Omega^2 r_s^2 \langle \beta \rangle V \quad (5)$$

after taking into account equation (3) and $\langle \beta \rangle = \tanh(k)/k$. The first term of equation (5) comprises the internal energy and the energy stored in magnetic field, while the second term accounts for the kinetic energy. A rise of the rotation frequency is anticipated during the compression, and the $\Omega \propto x_s^{-2}$ relation can be deduced by assuming the plasma angular momentum alone remains unchanged in conjunction with

the RR flow and density profile. In particular, the fluid inventory conservation $dN = 0$ provides

$$2\frac{dr_s}{r_s} + \frac{dl}{l} + \frac{dn_m}{n_m} + \frac{d\langle\beta\rangle}{\langle\beta\rangle} = 0, \quad (6)$$

and $dL = 0$ yields

$$\frac{d\Omega}{\Omega} + 4\frac{dr_s}{r_s} + \frac{dl}{l} + \frac{dn_m}{n_m} + \frac{d\langle\beta\rangle}{\langle\beta\rangle} = 0 \quad (7)$$

where the angular momentum $L = \int \rho\Omega r^2 dV = m_i n_m \Omega r_s^2 \langle\beta\rangle V/2$, $N = \int n dV = n_m \langle\beta\rangle V$ and $V = \pi r_s^2 l$. Consequently $d\Omega/\Omega + 2dr_s/r_s = 0$ can be obtained from combining equation (6) and equation (7). Due to the conversion of a fraction of work done on the separatrix into kinetic energy during the compression, the pressure is expected to reduce relatively to the situation in absence of initial flow, thereby leading to a less effective compressional heating. It is noted that while $dL = 0$ holds as the FRC maintains steady equilibrium during compression, this condition is not met in the dynamic compression process when the FRC deviates from its equilibrium state, as discussed next in section 2.2.

2.2. Angular momentum conservation in dynamic compression

In a toroidally rotating plasma system in absence of any direct deposition from external angular momentum source such as the neutral beam injection, the angular momentum conservation is governed by the equation:

$$\frac{dL}{dt} = \tau_{z,tot} \quad (8)$$

and

$$\tau_{z,tot} = - \int r \hat{\theta} \cdot (\nabla \cdot \overset{\leftrightarrow}{T}) dV, \quad (9)$$

where $L = \int r \rho u_\theta dV$ is the axial angular momentum of plasma and $\tau_{z,tot}$ represents the total axial torque [34]. $\overset{\leftrightarrow}{T}$ is the stress tensor

$$\overset{\leftrightarrow}{T} = \rho \vec{u} \vec{u} + \left(p + \frac{B^2}{2\mu_0}\right) \overset{\leftrightarrow}{I} - \frac{\vec{B} \vec{B}}{\mu_0} + \overset{\leftrightarrow}{\Pi}, \quad (10)$$

$\overset{\leftrightarrow}{\Pi}$ is the viscosity tensor and $\overset{\leftrightarrow}{I}$ is the unit tensor. During the dynamic compression, the total torque is primarily composed of the electromagnetic torque $\tau_{z,EM}$ corresponding to the Maxwell stress tensor $\overset{\leftrightarrow}{T}_M = -B^2/(2\mu_0) \overset{\leftrightarrow}{I} + \vec{B} \vec{B}/\mu_0$ and the torque $\tau_{z,R}$ induced by the Reynold stress tensor $\overset{\leftrightarrow}{T}_R = \rho \vec{u} \vec{u}$

$$\tau_{z,tot} \approx \tau_{z,EM} + \tau_{z,R}, \quad (11)$$

where

$$\tau_{z,EM} = \int \frac{r}{\mu_0} B_\theta \vec{B} \cdot \vec{n} dS \quad (12)$$

and

$$\tau_{z,R} = - \int r \rho u_{\theta} \vec{u} \cdot \vec{n} dS \quad (13)$$

within a cylindrical volume enclosed by the surface with unit normal vector \vec{n} . Due to the dynamic nature of the compression process, the nonzero B_{θ} driven by the differential rotation with nonuniform rotation frequency Ω [35], and the finite radial compression velocity $\vec{u} \cdot \vec{n}$ can both enable violation of the condition $dL = 0$ that is assumed in the 1D quasi-static adiabatic compression model in the previous subsection 2.1. The consequence of the dynamic angular momentum conservation with $dL \neq 0$ will be demonstrated and analyzed along with the simulation results presented in section 3.

3. Numerical simulation

3.1. Simulation model and setup

The simulations in this work are conducted using the NIMROD code [28], which employs the finite element discretization in the (r, z) plane and Fourier series decomposition in the θ direction. To compare with Spencer's scaling laws, the resistive single-fluid MHD equations are solved

$$\frac{\partial n}{\partial t} + \nabla \cdot (n\vec{u}) = 0, \quad (14)$$

$$\rho \left(\frac{\partial \vec{u}}{\partial t} + \vec{u} \cdot \nabla \vec{u} \right) = \vec{J} \times \vec{B} - \nabla p - \nabla \cdot \overset{\leftrightarrow}{\Pi}, \quad (15)$$

$$\frac{n}{\gamma - 1} \left(\frac{\partial}{\partial t} + \vec{u} \cdot \nabla \right) T = -p \nabla \cdot \vec{u} + Q, \quad (16)$$

$$\frac{\partial \vec{B}}{\partial t} = -\nabla \times \vec{E}, \quad (17)$$

$$\vec{E} = -\vec{u} \times \vec{B} + \eta \vec{J}, \quad (18)$$

where n is the plasma number density, \vec{u} the plasma velocity, ρ the mass density, \vec{J} the current density, \vec{B} the magnetic field, p the pressure, $\overset{\leftrightarrow}{\Pi}$ the viscosity tensor, $T = T_i + T_e$ the total temperature, \vec{E} the electric field, η the resistivity and $Q = \eta J^2$ represents the resistive heating power. Employing the Spitzer's resistivity model, a core plasma resistivity corresponding to a Lundquist number of 6×10^4 is initialized, with the wall radius adopted as the relevant length scale. Minimal values of viscosity and density diffusivity are kept to ensure the numerical stability and convergence of the simulation results. An isotropic viscosity corresponding to the Reynolds number of 2×10^4 is applied. A parallel viscosity of $10^4 \text{m}^2/\text{s}$ is used as well following previous FRC simulations [36, 37, 19]. Moreover, a supplementary ohmic heating introduced in the simulations is two orders of magnitude lower than the internal energy. The magnetic compression boundary condition is externally applied on the $r = r_w$ boundary, where the compression field B_z ramps with time [19].

The initial FRC equilibrium before the compression is prepared by numerically solving the Grad-Shafranov (GS) equation with toroidal rotation, using the extended NIMEQ code [38, 39]. The equilibrium exhibits variations in pressure and magnetic flux distributions due to the toroidal flow effects [40, 41], where the pressure and the mass density are functions of both ψ and r [38, 42, 43]

$$p(\psi, r) = p_0(\psi) \exp \left[\frac{m_i r_o^2 \Omega^2}{2T} \left(\frac{r^2}{r_o^2} - 1 \right) \right], \quad (19)$$

$$\rho(\psi, r) = \rho_0(\psi) \exp \left[\frac{m_i r_o^2 \Omega^2}{2T} \left(\frac{r^2}{r_o^2} - 1 \right) \right], \quad (20)$$

with $p_0(\psi)$ and $\rho_0(\psi)$ being the static equilibrium pressure and mass density profiles respectively. The initial equilibrium flow is thus anticipated to have an indirect impact on the compression process through the modifications to initial equilibrium itself. Detailed analyses of flow effects on the compression will be conducted in subsequent simulations in the range of $\alpha < 1.5 - 2$, where $\alpha = \langle u_\theta \rangle / u_*$ [44, 45] and $u_* = \langle J / (en) \rangle$ are averages over the middle plane. This range of equilibrium flow speeds encompass the regime observed in the majority of FRC experiments and simulations (e.g. [20, 23, 25, 46]). The influence of different toroidal rotation profiles on the compression scaling laws is also studied, including the rigid rotation, a single-peaked rotation profile with the maximum flow speed near the O-point [25], and a double-peaked rotation profile similar to that in Ref. [45], using a cubic function and a Gaussian shaped function for $\Omega(\psi)$ respectively [39, 42].

3.2. Effects of initial rigid rotation

We first compare the simulation results on the magnetic compression scalings between a static initial equilibrium and those with an initial rigid rotation. The simulations in absence of an initial flow are performed following the earlier simulation setups [19], and the corresponding equilibrium magnetic flux contours are presented in figure 1(b). The initial steady equilibrium shares the same $p_0(\psi)$ shown in equation (19) as the static equilibrium when solving the GS equation, where $p_0(\psi)$ is constant outside the separatrix. In magnetic compression experiments a large initial x_s is preferred for high efficiency [13], and $x_s \sim 1$ is adopted as an optimal case in the simulations. The maximum equilibrium rotation frequency $\Omega_{0m} \sim 0.23\Omega_A$ adopted in simulations corresponds to $\alpha \sim 1.5$ under the RR flow, where $\Omega_A = V_A/r$, $\Omega_{0m}/\Omega_A = V_{0m}/V_A$, V_{0m} is the initial maximum magnitude of the toroidal velocity V_t , which is in the co-rotating direction counter to the θ -direction, i.e. $V_t = -u_\theta$, and $V_A = B_w / (\mu_0 m_i n_m)^{1/2}$ is the characteristic Alfvén velocity of the initial equilibrium. The RR flow slightly alters the initial equilibrium flux shape with this flow speed (figure 1(b)). Moreover, the standard calculations are only limited to 2D because the 2D simulations yield the same results as the 3D cases when no initial perturbations are applied to the internal simulation domain, thereby confirming the numerical accuracy of the simulations.

The p_m , T_m and n_m at the $z = 0$ middle plane during the compression process in simulations are plotted in figure 2 for comparison with the 1D scalings shown in table 1. The subscripts “1” and “2” denote the equilibrium state before compression and the final state at the corresponding compression ratio respectively. As can be seen from figure 2, the presence of an initial rigid rotation is responsible for a reduction in the maximum temperature of the compressed FRC. Both the pressure and density are also reduced within the regime $B_{w2}/B_{w1} < 5$ in comparison to the case with the static equilibrium. Figure 3 shows that at $t = 30\mu s$ with $B_{w2}/B_{w1} \sim 4.7$, the presence of initial RR flow leads to a higher density outside the separatrix and slightly lower density inside relative to the case in absence of initial toroidal flow. The centrifugal force can retard the radial inward concentration of the density during compression, which is similarly observed in the tilt mode simulations [47]. The compressed FRC gradually deviates from the elongated separatrix shape assumed in the 1D adiabatic model during compression, and the simulation cases with and without initial flow show negligible difference in the pressure scaling after $B_{w2}/B_{w1} > 5$. The conversion of a fraction of the compressional magnetic energy into the toroidal kinetic energy leads to overall less effective heating. Consequently the FRC with initially rigid rotation (figure 2) maintains a poloidal flux approximately 7% lower than that without initial flow at $B_{w2}/B_{w1} \sim 8$. Since B_w is the sum of the externally applied field and that induced by plasma, the B_w shown in figure 2(a) exhibits discrepancy between the two simulation cases despite identical boundary conditions. The axial contraction of the FRC with initial rigid rotation is slightly faster before $B_{w2}/B_{w1} < 3$. For the other two initial radial profiles of toroidal rotation shown in figure 7, the axial contraction of the FRC during compression is somewhat slower than the case without initial flow. The two simulation cases in figure 2 have a peaked equilibrium density profile with $n(r = 0)/n_m \sim 0.5$, resembling the RR density profile shown in equation (4) with $k = 0.9$. Whereas different density profiles have been demonstrated to primarily affect the density and temperature scalings for the magnetic compression of the initially static FRC equilibrium [19], the toroidal flow effects induced by an initially rigid rotation are found similar on scalings for both the uniform and the peaked initial density profiles.

The quasi-static 1D model in section 2.1 predicts a monotonic rise in toroidal rotation and kinetic energy, thus the consequent compression scalings are expected to significantly deviate from the Spencer theory [17]. However, in simulations the maximum toroidal velocity, along with the toroidal flow induced deviations in pressure and length scalings from the Spencer theory initially rises but subsequently decreases as shown in figures 2 and 4. This result may be understood by the mitigating effects of the electromagnetic torque in equation (12) as explained next.

It is noted that a significant B_θ arises during the compression as figure 5 demonstrates. For the cylinder with a length between $-z_{end}$ and z_{end} and a radius of r_{end} , the axial electromagnetic torque from each end surface of the cylinder can be

expressed as

$$\tau_1 = \int_0^{r_{end}} \frac{2\pi}{\mu_0} r^2 B_\theta B_z dr, \quad (21)$$

whereas the torque from the wall surface of the cylinder is

$$\tau_2 = \int_{-z_{end}}^{z_{end}} \frac{2\pi}{\mu_0} r_{end}^2 B_\theta B_r dz. \quad (22)$$

Given the odd symmetry of B_θ about the $z = 0$ middle plane shown in figure 5, a net total electromagnetic torque can be evaluated as $\tau_{z,EM} = 2\tau_1 + \tau_2$.

The electromagnetic torque $\tau_{z,EM}$ acting on the cylinder enclosing the FRC region during compression is obtained for $r_{end} = 1.3r_s$ and $z_{end} = 1.6\text{m}$ (figure 6). The $B_z > 0$ in the open field line region corresponds to an initial co-rotating flow $V_t > 0$ that is counter to the θ direction in our simulations, and $\tau_{EM} = -\tau_{z,EM} < 0$ highlighted in yellow in figure 6 thus represents a deceleration torque against the flow in the co-rotating direction. The electromagnetic torque τ_{EM} acts to decelerate the rotation as the velocity increases and accelerate it as the velocity decreases.

The electromagnetic torque oscillation in figure 6 also indicates an exchange between kinetic and magnetic energies, which correlates with the twisting and unwinding of magnetic field lines during the compression process. The amplitude of the torque goes down as the compression becomes less dynamic. The energy exchanges primarily between the toroidal components B_θ and u_θ , with minimal impact on the compression process in the poloidal plane. The torque modulates the variation of toroidal velocity and produces a pronounced flow shear near the separatrix, where substantial plasma outside the separatrix rotates in the opposite direction with $V_t < 0$ (figure 4). The rotation reversal continuously decelerates the velocity near the separatrix even as the torque τ_{EM} oscillates down to a negligible magnitude. In this way, the electromagnetic torque is able to divert away the toroidal flow effects on compression scalings.

3.3. Results with initially sheared rotation

Although the rigid rotation maybe straightforward and readily amenable to analytical solutions, significant flow shear is anticipated in more realistic FRC equilibria. Figure 7(a) illustrates two additional types of initial toroidal rotation profiles, with their corresponding equilibrium poloidal flux displayed in figure 7(b) and 7(c). Variations in rotation profiles can result in distinct distributions of equilibrium parameters. Specifically, in our simulations the single-peaked toroidal rotation profile elongates the internal poloidal flux contours, whereas the double-peaked toroidal rotation profile renders the core flux structure more oblate. These flow-profile induced variations in the initial equilibria can indirectly alter the magnetic compression scalings, as demonstrated in figure 8. The $\Omega_{0m} \sim 0.35\Omega_A$ in the single-peaked rotation profile corresponds to $\alpha \sim 2$, and in the case of the double-peaked rotation profile the $\Omega_{0m} \sim 0.37\Omega_A$ corresponds to $\alpha \sim 1.8$. The maximum density evolutions in both initial rotation profile cases exhibit similarities, which also agree with the case without initial flow

until $B_{w2}/B_{w1} \gtrsim 5$. For the cases with the initial single-peaked rotation profile, however, a more significant temperature reduction is observed after $B_{w2}/B_{w1} > 4$ and $\Omega_{0m} > 0.22\Omega_A$. This plasma temperature drop is reminiscent of the results in the FRX-C/LSM compression experiments [15]. The single-peaked rotation profile progressively elongates the core FRC equilibrium structure as the initial flow speed rises, leading to the formation of a thin and elongated current sheet. This elongation in the initial equilibrium structure is prone to field line tearing during compression, as shown in figure 9. In contrast, the initial oblate core FRC structure associated with the double-peaked rotation profile inhibits the tearing mode and the subsequent plasma temperature drop during compression.

The extent to which the pressure and radius scalings are affected by toroidal flow effects is not as pronounced as it is for the temperature scaling. Basically increasing the initial flow speed results in only slightly reduced FRC pressure and radius during compression. Such effects of the initial flows persist when considering the field line tearing during compression in cases with an initially single-peaked toroidal rotation profile, as illustrated in figure 10. Contrary to the compressed FRC with the initial rigid rotation, the compressed FRCs exhibit slower axial contraction following the initial single-peaked and double-peaked rotation profiles, particularly in cases where tearing modes appear, as can be seen from figures 10 and 11. In scenarios featuring initial single-peaked and double-peaked rotation profiles, the flow effects on compression scalings under different initial density profiles show qualitative similarities except the density scaling. The density scaling is influenced by both the initial rotation and density profiles. For simulation cases with a uniform density profile (figure 11), the density scaling remains generally lower compared to cases without initial flow before $B_{w2}/B_{w1} < 5$. By contrast in cases with initial peaked density profile where $n(r=0)/n_m \sim 0.5$ (figure 8), the density scaling aligns closely with the case without initial flow during $B_{w2}/B_{w1} < 5$. Nevertheless, different density profiles do not significantly modify the overall flow effects on the compression scalings.

An enhanced toroidal rotation gradient near $r = r_s$ is induced during the compression, as can be seen from figure 12 for the case with initial double-peaked rotation profile and $\Omega_{0m} \sim 0.37\Omega_A$. The flow rotation frequency increases rapidly alongside the decreasing FRC radius. The rotation frequency rises to $\sim 6.4\Omega_1$ at $t = 20\mu s$ and $r \sim 0.13m$, and further to $\sim 15\Omega_1$ at $t = 30\mu s$ and $r \sim 0.02m$. The magnitude of the toroidal rotation first increases and then decreases, which may partially explain the observed deviations in pressure and length scalings due to flow that is characterized by a rise and the subsequent fall during compression, as shown in figure 11. Throughout the compression process, the pressure profile peaks around the r_o , and the temperature reaches its maximum between the O -point and r_s , whereas the maximum density accumulates at $r = 0$ after $t > 10\mu s$. The discrepancy in the peak locations of the pressure, temperature and density profiles may account for their differences from the Spencer theory predictions. The steep gradient of the pressure and temperature profiles within r_s can be attributed to the adiabatic limit of equation (16)

in the absence of thermal conduction and due to a slower compression rate than the maximum acoustic speed. Despite a wide range of variation in the toroidal rotation profile during compression, the shapes of the pressure, density and temperature profiles at the middle plane do not undergo fundamental changes compared to the case in absence of initial flow.

4. Discussion and conclusions

Investigations into the toroidal flow effects on the magnetic compression scalings have been conducted. The MHD simulations employing the NIMROD code, which spans a range of initial rotation observed in the majority of FRC experiments and simulations, are compared with the simulation results and the Spencer scaling laws for static initial equilibriums. Various representative initial rotation and density profiles have also been considered. Basically the initial flow can affect the compression scalings through two mechanisms: one is the alteration of the compression process itself, resulting in a reduced compressional heating efficiency; the other is through reshaping the equilibrium distributions, thereby indirectly influencing the scalings particularly on the temperature, density and length evolutions.

In the presence of initial rotation, the pressure scaling remains essentially same in comparison to the cases in absence of initial flow. The initial flow does tend to lower the temperature in the compressed state. A more significant temperature drop during the compression, reminiscent of the experimental results of the FRX-C/LSM device [15], can be induced by the field line tearing which is more likely to take place when the flow effects elongate the core flux contours of the initial FRC equilibrium. Flow effects on the density scaling rely on both the initial flow and density profiles. Generally speaking, with initial flow the density scaling is slightly lower before $B_{w2}/B_{w1} < 5$, but becomes higher after $B_{w2}/B_{w1} > 5$. The radius scaling can be influenced by flow effects with a deviation from the initially static case less than 15%. The length scaling demonstrates an increase and it shows a faster axial contraction when $B_{w2}/B_{w1} < 3$ with the initially rigid rotation. In summary, for initially rotating FRCs, the pressure and the radius scalings are nearly the invariant from the Spencer scalings for the magnetic compression ratio up to $B_{w2}/B_{w1} \sim 6$.

Such an invariance has been found a natural consequence of the dynamic angular momentum conservation due to the generation of a significant electromagnetic torque during the compression process, which acts on the plasma to oppose the acceleration of its toroidal rotation in general. A pronounced flow shear induced by the electromagnetic torque can continue to slow down the plasma rotation near the separatrix, even after the electromagnetic torque decays to negligible level. The electromagnetic torque oscillations during the compression indicate the twisting and unwinding of magnetic field lines, suggesting a dynamic exchange between kinetic and magnetic energies, which primarily involves the toroidal components u_θ and B_θ , and has minimal influence on the magnetic compression dynamics within the poloidal plane. The generation of the B_θ

by dynamo effects and the corresponding electromagnetic torque signifies the dynamic nature of compression missing in the 1D adiabatic model, as well as a key difference between the simulation and the quasi-static theoretical approaches.

The initial toroidal flow is expected to influence the FRC stability during compression. For example, toroidal flow is believed to excite the interchange modes driven by centrifugal force, particularly the $n = 2$ rotational instability. On the other hand, our simulations with initial toroidal flow consistently show substantial B_θ and dynamically evolving rotation profiles with strong flow shear, which is generally considered beneficial for the FRC stability. Whereas the focus here is on the compression scalings, the stability of the compressed FRCs, particularly in presence of the evolving flow profiles, is an important topic that is planned for future investigation.

5. Acknowledgement

This work was supported by the National Key Research and Development Program of China (Grant No. 2019YFE03050004), the National Natural Science Foundation of China (Grant No. 51821005), and the U.S. Department of Energy (Grant No. DE-FG02-86ER53218). The computing work in this paper was supported by the Public Service Platform of High Performance Computing by Network and Computing Center of HUST. The authors are very grateful for the supports from the NIMROD team and the J-TEXT team.

References

- [1] Tuszewski M. 1988 Field reversed configurations *Nucl. Fusion* **28** 2033
- [2] Rej D.J. *et al* 1986 Experimental studies of field-reversed configuration translation *Phys. Fluids* **29** 852–862
- [3] Schwarzeimer J.L. *et al* 1983 Magnetohydrodynamic equilibrium and stability of field-reversed configurations *Phys. Fluids* **26** 1295
- [4] Slough J.T. *et al* 1995 Transport, energy balance, and stability of a large field-reversed configuration *Phys. Plasmas* **2** 2286–2291
- [5] Steinhauer L.C. 1996 FRC 2001: a white paper on FRC development in the next five years *Fus. technol.* **30** 116
- [6] Liao H. *et al* 2022 First direct experimental evidence of the merging of two colliding field reversed configurations *Plasma Phys. Control. Fusion* **64** 115003
- [7] Liao H. *et al* 2022 The dynamic axial compression of FRC with high-speed translated θ -pinch plasma *Plasma Phys. Control. Fusion* **64** 105015
- [8] Sekiguchi J. *et al* 2018 Super-Alfvénic translation of a field-reversed configuration into a large-bore dielectric chamber *Rev. Sci. Instrum.* **89** 013506
- [9] Kobayashi D. and Asai T. 2021 Experimental evidence for super-Alfvénic acceleration of the field-reversed configuration due to a magnetic pressure gradient *Phys. Plasmas* **28** 022101
- [10] Asai T. *et al* 2021 Observation of self-organized FRC formation in a collisional-merging experiment *Nucl. Fusion* **61** 096032
- [11] Asai T. *et al* 2019 Collisional merging formation of a field-reversed configuration in the FAT-CM device *Nucl. Fusion* **59** 056024

- [12] Gota H. *et al* 2021 Overview of C-2W: high temperature, steady-state beam-driven field-reversed configuration plasmas *Nucl. Fusion* **61** 106039
- [13] Slough J. *et al* 2011 Creation of a high-temperature plasma through merging and compression of supersonic field reversed configuration plasmoids *Nucl. Fusion* **51** 053008
- [14] Steinhauer L.C. 2011 Review of field-reversed configurations *Phys. Plasmas* **18** 070501
- [15] Rej D.J. *et al* 1992 High-power magnetic-compression heating of field-reversed configurations *Phys. Fluids B: Plasma Phys.* **4** 1909
- [16] Kirtley D. and Milroy R. 2023 Fundamental scaling of adiabatic compression of field reversed configuration thermonuclear fusion plasmas *J. Fusion Energy* **42** 30
- [17] Spencer R.L. *et al* 1983 Adiabatic compression of elongated field-reversed configurations *Phys. Fluids* **26** 1564
- [18] Woodruff S. *et al* 2008 Adiabatic compression of a doublet field reversed configuration (FRC) *J. Fusion Energy* **27** 128
- [19] Ma Y. *et al* 2023 Mhd simulation on magnetic compression of field reversed configurations with NIMROD *Nucl. Fusion* **63** 046017
- [20] Belova E.V. *et al* 2005 Numerical study of the formation, ion spin-up and nonlinear stability properties of field-reversed configurations *Nucl. Fusion* **46** 162
- [21] Belova E.V. *et al* 2001 Numerical study of global stability of oblate field-reversed configurations *Phys. Plasmas* **8** 1267–1277
- [22] Belova E.V. *et al* 2003 Kinetic effects on the stability properties of field-reversed configurations. I. Linear stability *Phys. Plasmas* **10** 2361–2371
- [23] Belova E.V. *et al* 2004 Kinetic effects on the stability properties of field-reversed configurations. II. Nonlinear evolution *Phys. Plasmas* **11** 2523–2531
- [24] Harris W.S. *et al* 2009 Ion flow measurements and plasma current analysis in the Irvine field reversed configuration *Phys. Plasmas* **16** 112509
- [25] Ono Y. *et al* 2003 Spontaneous and artificial generation of sheared-flow in oblate FRCs in TS-3 and 4 FRC experiments *Nucl. Fusion* **43** 649
- [26] Glasser A.H. *et al* 1999 The NIMROD code: a new approach to numerical plasma physics *Plasma Phys. Control. Fusion* **41** A747
- [27] Sovinec C.R. *et al* 2003 NIMROD: A computational laboratory for studying nonlinear fusion magnetohydrodynamics *Phys. Plasmas* **10** 1727–1732
- [28] Sovinec C.R. *et al* 2004 Nonlinear magnetohydrodynamics simulation using high-order finite elements *J. Comput. Phys.* **195** 355
- [29] Armstrong W.T. *et al* 1981 Field-reversed experiments (FRX) on compact toroids *Phys. Fluids* **24** 2068
- [30] Lee K.Y. 2020 Generalized radial profile of field-reversed configurations based on symmetrical properties *Nucl. Fusion* **60** 046010
- [31] Intrator T.P. *et al* 2008 Adiabatic model and design of a translating field reversed configuration *Phys. Plasmas* **15** 042505
- [32] Intrator T.P. *et al* 2008 Physics basis and progress for a translating FRC for MTF *J. Fusion Energy* **27** 57
- [33] Tuszewski M. 1988 A semiempirical formation model for field-reversed configurations *Phys. Fluids* **31** 3754
- [34] Pustovitov V.D. 2011 Integral torque balance in tokamaks *Nucl. Fusion* **51** 013006
- [35] Guzdar P.N. *et al* 1985 The role of magnetic reconnection and differential rotation in spheromak formation *Phys. Fluids* **28** 3154–3166
- [36] Milroy R.D. *et al* 2010 Extended magnetohydrodynamic simulations of field reversed configuration formation and sustainment with rotating magnetic field current drive *Phys. Plasmas* **17** 062502
- [37] Macnab A.I.D. *et al* 2007 Hall magnetohydrodynamics simulations of end-shortening induced rotation in field-reversed configurations *Phys. Plasmas* **14**
- [38] Li H. and Zhu P. 2021 Solving the Grad–Shafranov equation using spectral elements for tokamak

- equilibrium with toroidal rotation *Comput. Phys. Commun.* **260** 107264
- [39] Howell E.C. and Sovinec C.R. 2014 Solving the Grad–Shafranov equation with spectral elements *Comput. Phys. Commun.* **185** 1415
- [40] Evangelias A. and Throumoulopoulos G.N. 2016 Axisymmetric equilibria with pressure anisotropy and plasma flow *Plasma Phys. Control. Fusion* **58** 045022
- [41] Guazzotto L. and Paccagnella R. 2009 Magnetic field profiles in fusion plasmas in the presence of equilibrium flow *Plasma Phys. Control. Fusion* **51** 065013
- [42] Li H. and Zhu P. 2021 Formation of edge pressure pedestal and reversed magnetic shear due to toroidal rotation in a tokamak equilibrium *Phys. Plasmas* **28** 054505
- [43] Aiba N. *et al* 2009 MINERVA: Ideal MHD stability code for toroidally rotating tokamak plasmas *Comput. Phys. Commun.* **180** 1282–1304
- [44] Harned D.S. and Hewett D.W. 1984 The origin of rotation in field-reversed configurations *Nucl. Fusion* **24** 201
- [45] Belova E.V. *et al* 2000 Numerical study of tilt stability of prolate field-reversed configurations *Phys. Plasmas* **7** 4996–5006
- [46] Ito Y. *et al* 1987 Ion rotational velocity of a field-reversed configuration plasma measured by neutral beam probe spectroscopy *The Physics of fluids* **30** 168–174
- [47] Milroy R.D. *et al* 1989 Nonlinear magnetohydrodynamic studies of the tilt mode in field-reversed configurations *Phys. Fluids B: Plasma Phys.* **1** 1225–1232

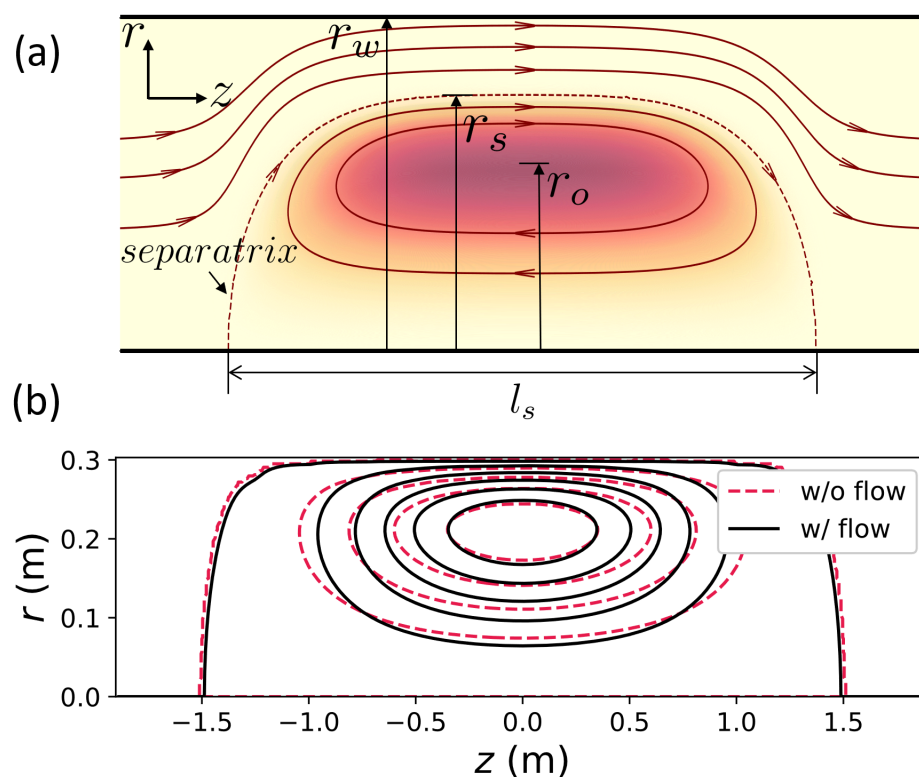


Figure 1. (a) A schematic plot of the FRC, where r_o , r_s , and r_w denote the radii of the magnetic axis, the separatrix, and the wall locations respectively, and l denotes the length of the FRC defined as the distance between the two separatrix-axis intersections. (b) The poloidal flux contours in the equilibriums in absence of flow (red) and in presence of the RR flow (black) respectively.

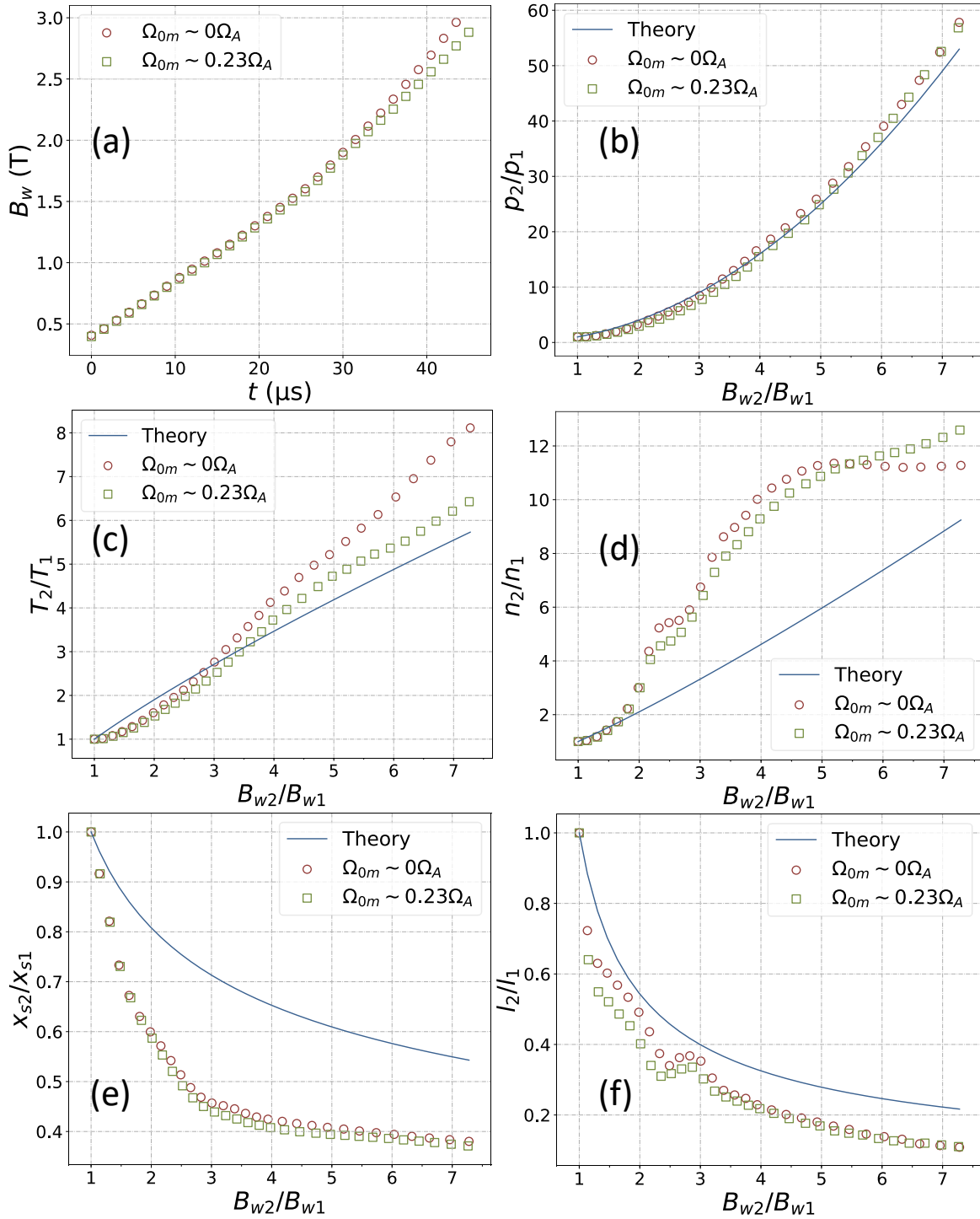


Figure 2. (a) The compression field B_w variation with time, the (b) pressure ratio p_2/p_1 , (c) temperature ratio T_2/T_1 , (d) density ratio n_2/n_1 , (e) radius ratio x_{s2}/x_{s1} and (f) length ratio l_2/l_1 as functions of the magnetic compression ratio B_{w2}/B_{w1} , obtained from Spencer's theory (blue lines) and the two simulation cases: one without flow (red circles) and the other with the initial rigid rotation (green rectangles).

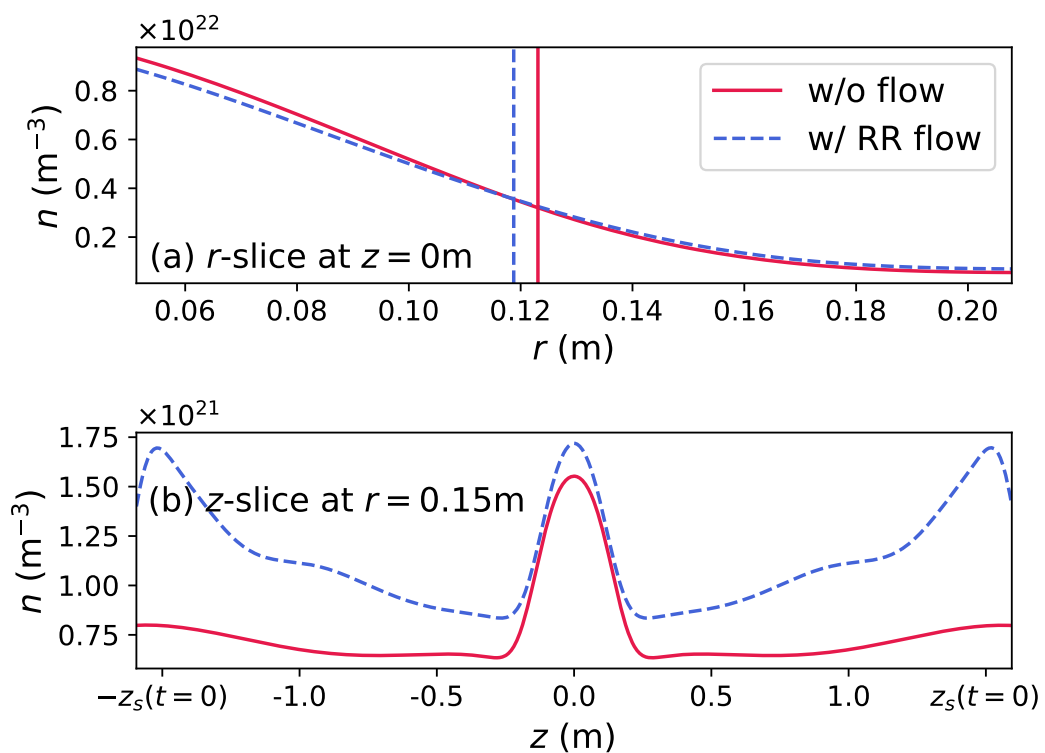


Figure 3. The density profiles at $t = 30 \mu\text{s}$ along (a) the $z = 0$ middle plane and (b) the $r = 0.15\text{m}$ axis. Vertical lines indicate $r = r_s$ for cases in absence of initial flow and with the initial rigid rotation. The simulations are same as the cases shown in figure 2.

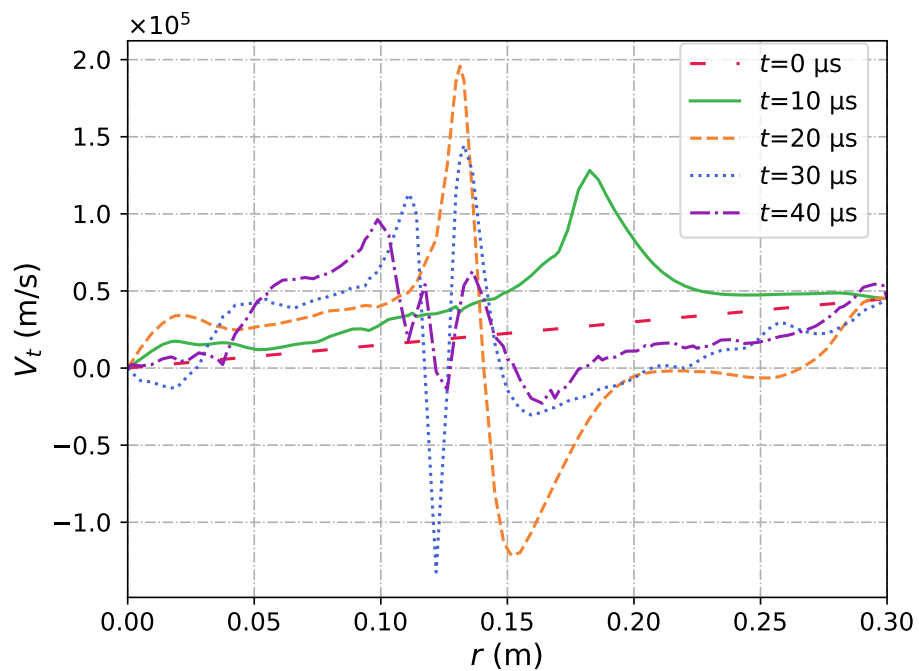


Figure 4. Radial profiles of toroidal velocity along the $z = 0$ middle plane at different times during compression. The simulation with initial rigid rotation is same as the case shown in figure 2.

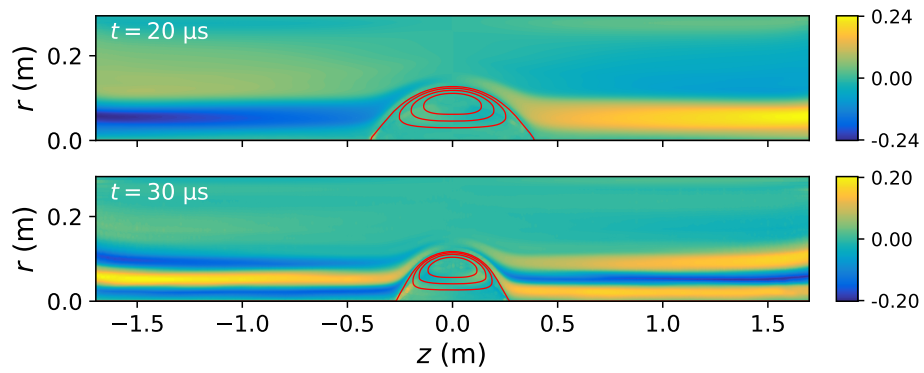


Figure 5. Contours of B_θ (colored) and poloidal flux (red) at $t = 20\mu\text{s}$ and $t = 30\mu\text{s}$ for the case with the initial rigid rotation. The simulation is same as the case shown in figure 2.

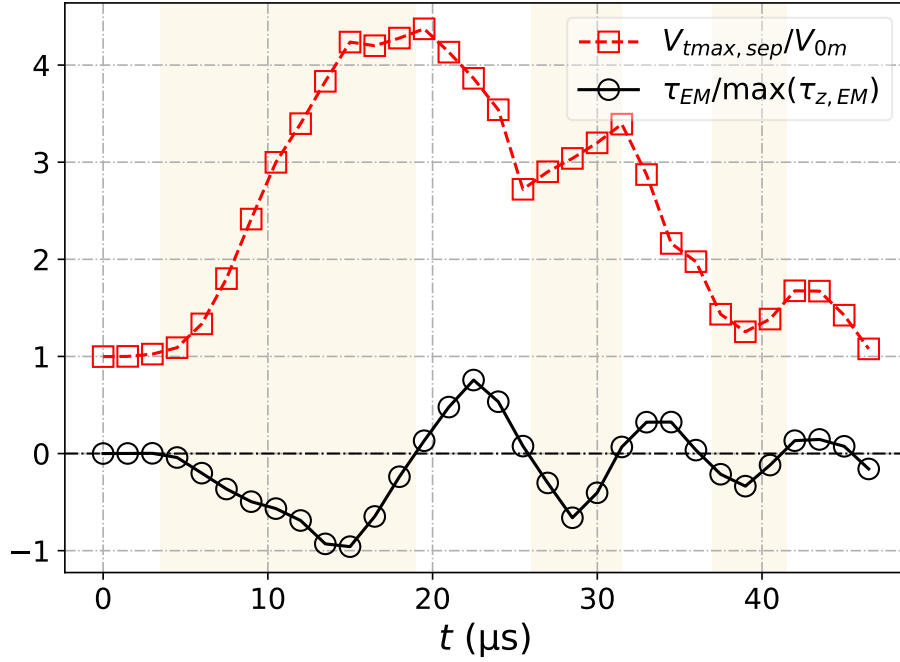


Figure 6. The time history of the normalized maximum toroidal velocity near the separatrix between $r = r_s$ and $r_{end} = 1.3r_s$ in the $z = 0$ middle plane (red) and the electromagnetic torque acting on the cylinder inside the volume specified by $0 \leq r \leq r_{end} = 1.3r_s$ and $-z_{end} \leq z \leq z_{end} = 1.6\text{m}$ (black) for the initial rigid rotation case, with $\tau_{EM} < 0$ shaded yellow. The simulation is same as the case shown in figure 2.

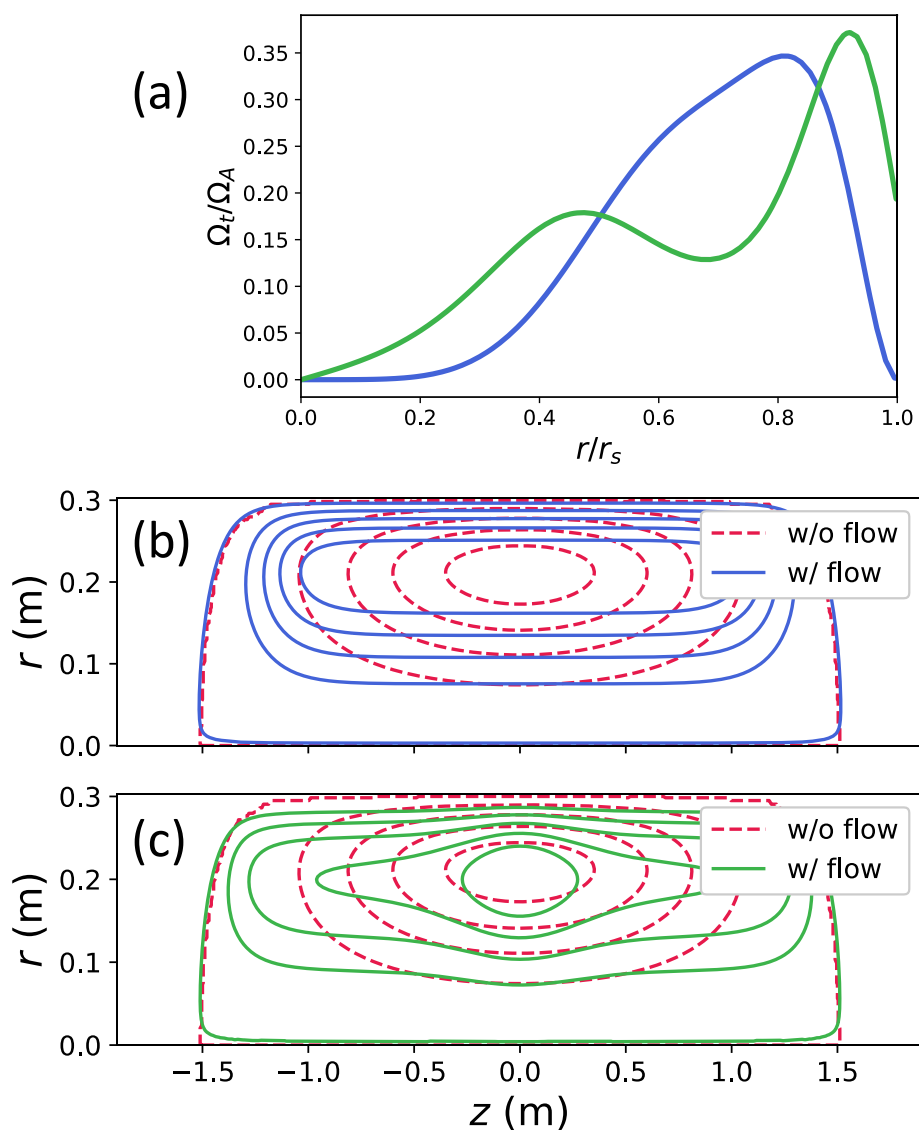


Figure 7. (a) The single- (blue) and double-peaked (green) initial toroidal rotation profiles at the $z = 0$ middle plane, and the corresponding equilibrium poloidal flux contours in presence of the (b) single- (blue) and the (c) double-peaked (green) rotation profiles in (a), in comparison to that of the equilibrium in absence flow (red).

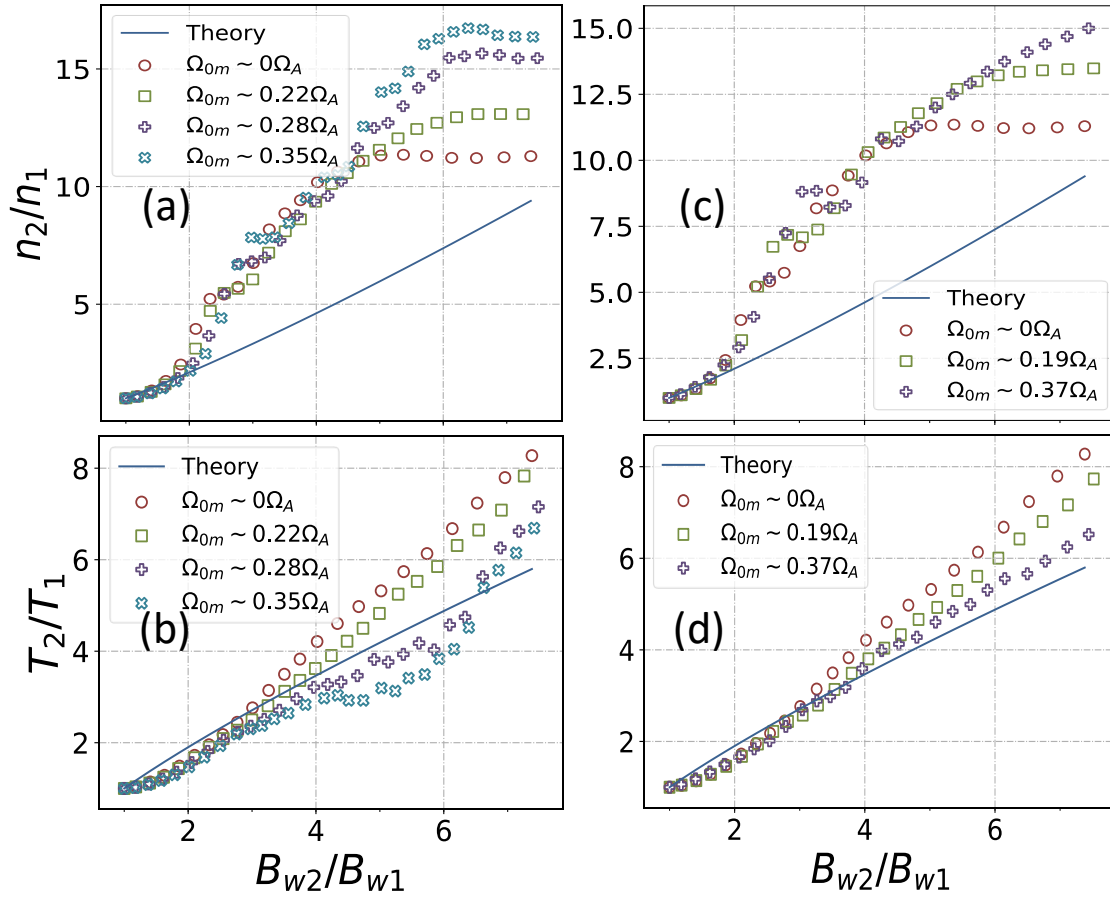


Figure 8. The compression ratio in (a) number density n_2/n_1 and (b) temperature T_2/T_1 in presence of initial single-peaked toroidal rotation profiles with various maximum rotation magnitude obtained from the Spencer theory (blue lines) and simulation results (symbols). The corresponding double-peaked rotation profile cases are shown in (c) and (d).

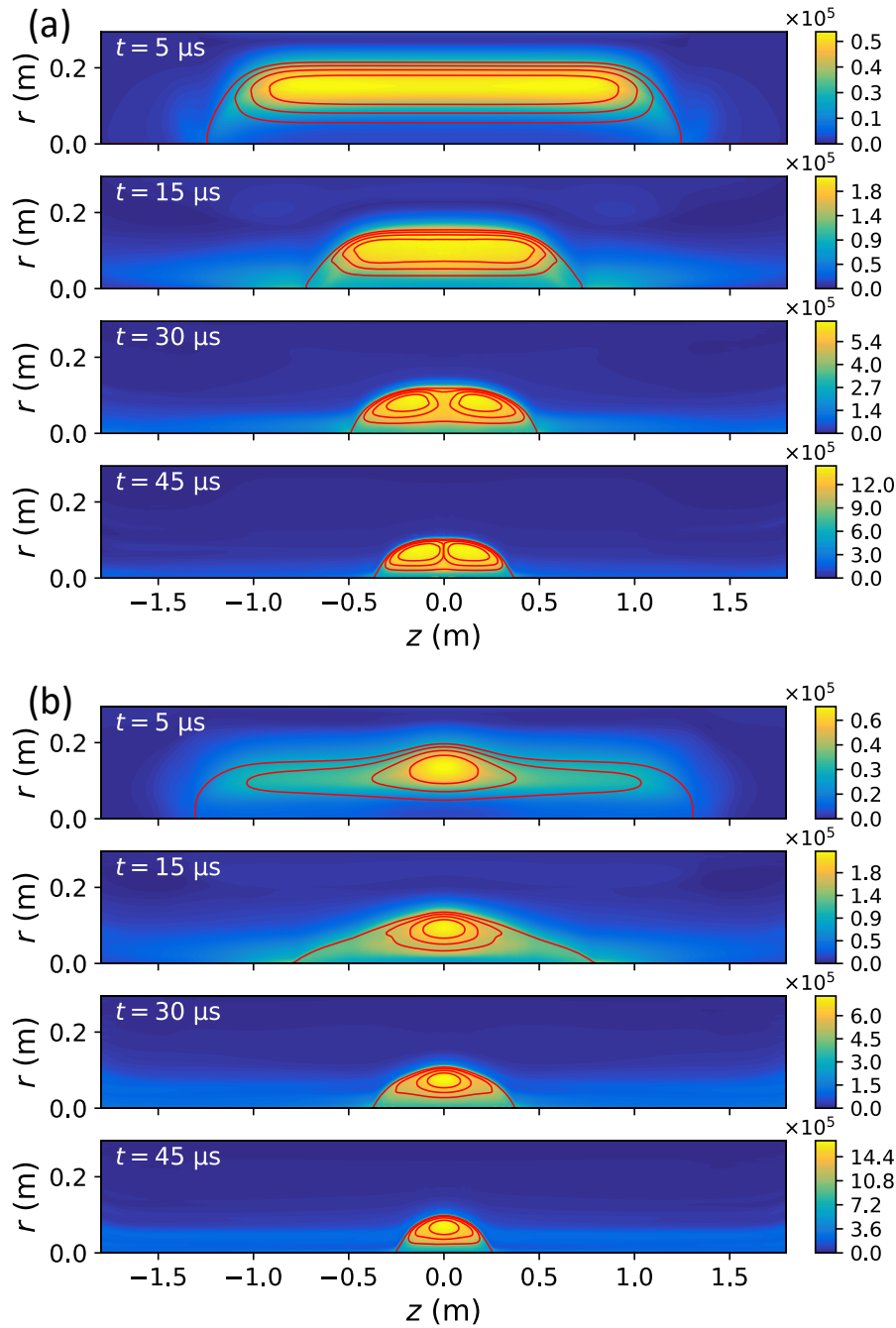


Figure 9. Pressure contours (colored) and poloidal flux contours (red) at different times during the compression for the same two cases shown in figure 8 with (a) initially single-peaked toroidal rotation profile and $\Omega_{0m} \sim 0.35\Omega_A$, (b) initially double-peaked toroidal rotation profile and $\Omega_{0m} \sim 0.37\Omega_A$.

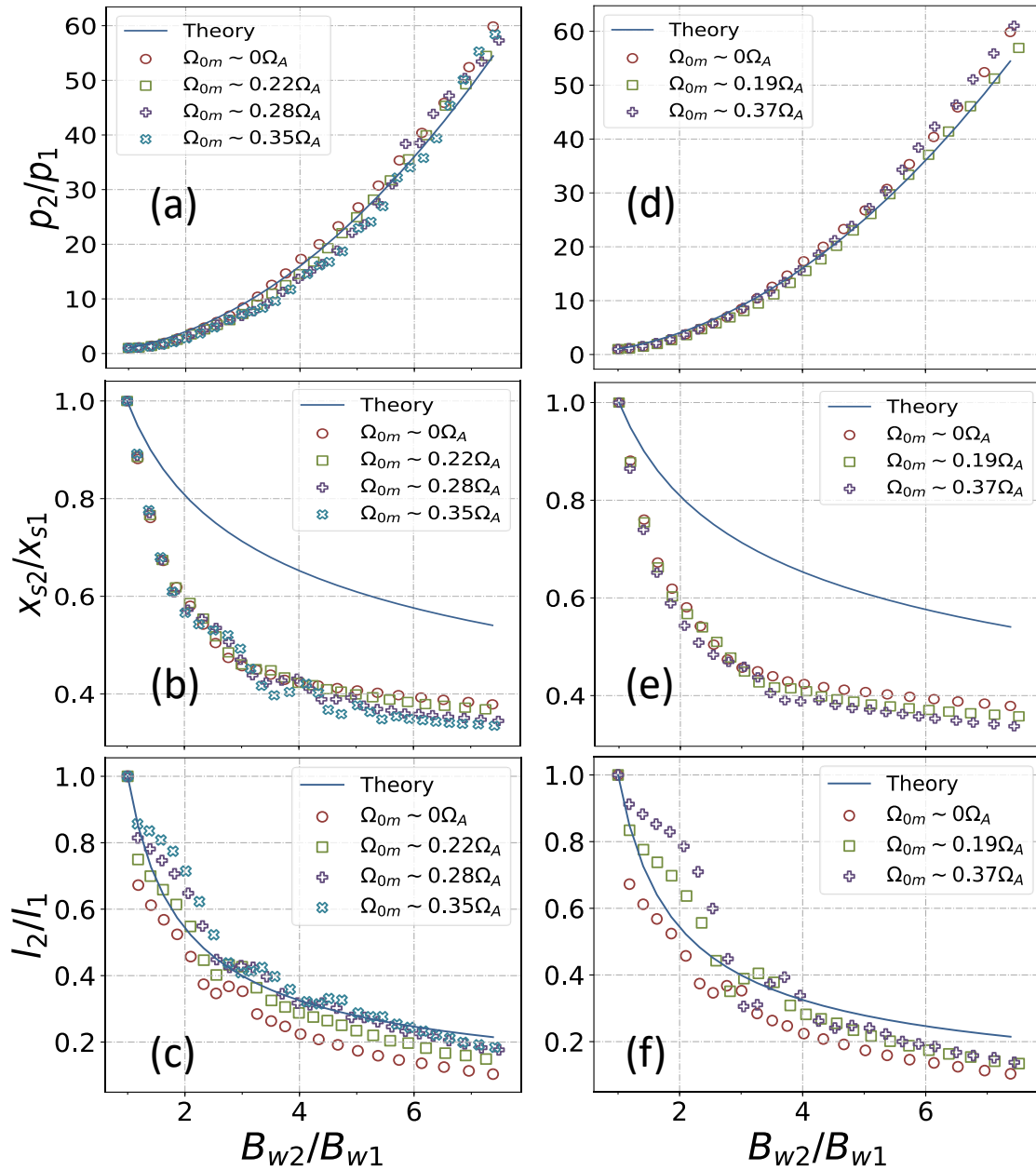


Figure 10. The compression ratio in (a) pressure p_2/p_1 , (b) radius x_{s2}/x_{s1} and (c) length l_2/l_1 in presence of initial single-peaked toroidal rotation profiles with various maximum rotation magnitude obtained from the Spencer theory (blue lines) and simulation results (symbols). The corresponding double-peaked rotation profile cases are shown in (d), (e) and (f). The simulations are same as the cases shown in figure 8.

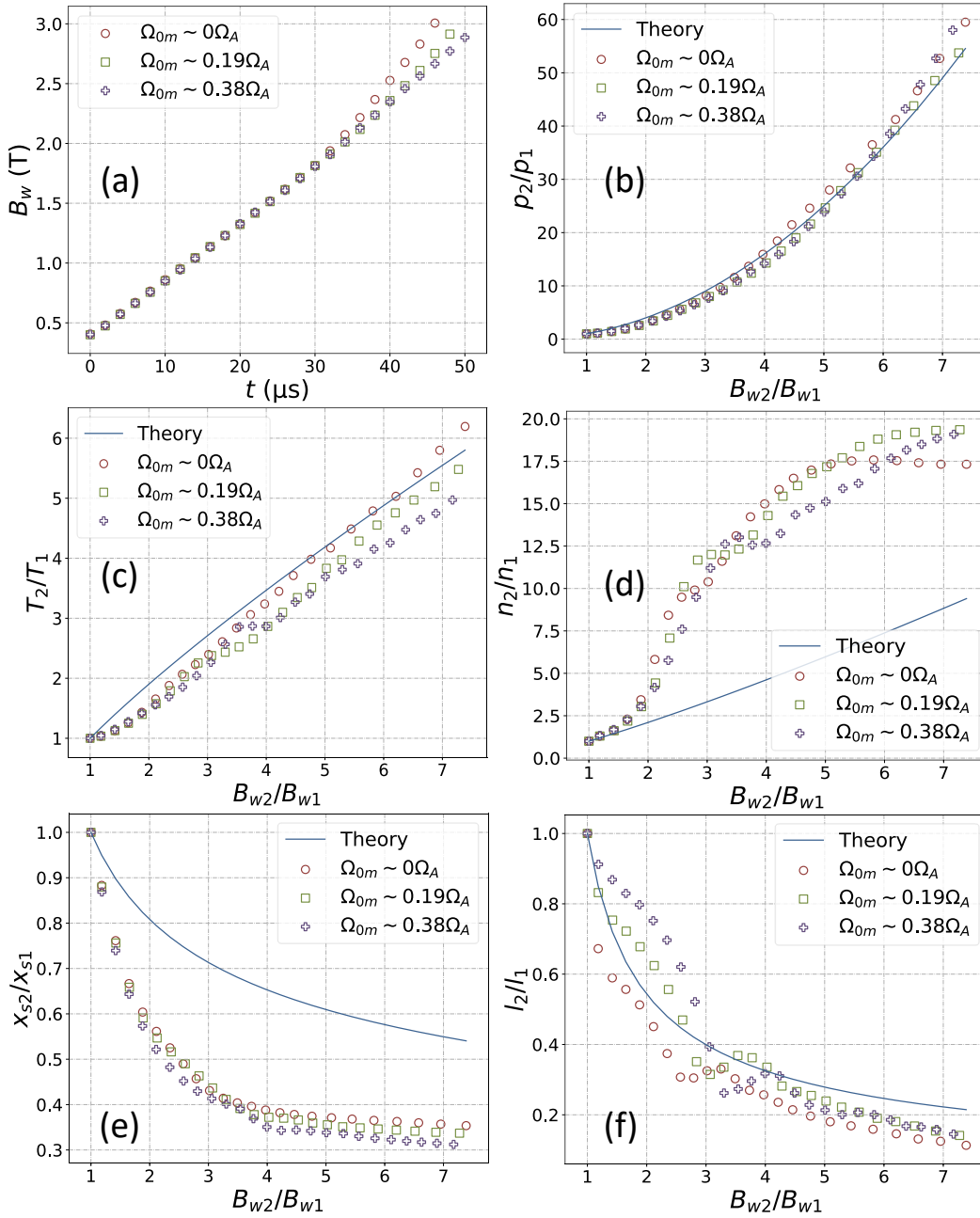


Figure 11. The comparisons between the Spencer's theory (blue lines) and simulation results with the initially double-peaked toroidal rotation profile. (a) The compression field B_w variation with time, the (b) pressure ratio p_2/p_1 , (c) temperature ratio T_2/T_1 , (d) density ratio n_2/n_1 , (e) radius ratio x_{s2}/x_{s1} and (f) length ratio l_2/l_1 as functions of the magnetic compression ratio B_{w2}/B_{w1} for different initial flow speeds. The simulation cases have an initially uniform density profile, differing from the cases in figures 2, 8 and 10 where an initially peaked density profile is used.

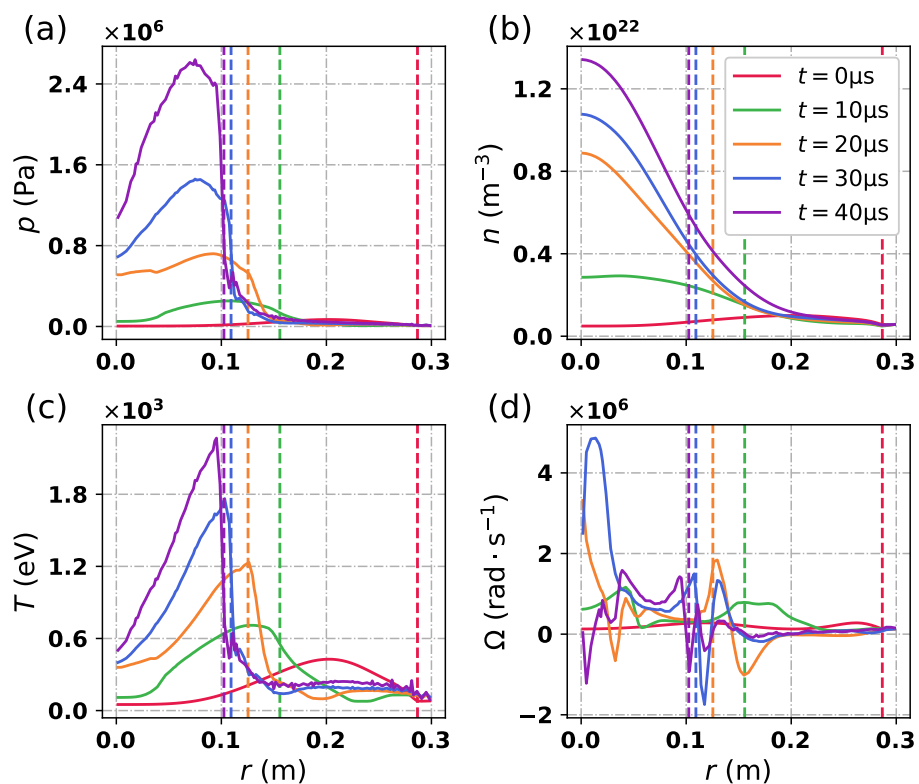


Figure 12. Radial profiles along the $z = 0$ middle plane of the (a) pressure, (b) density, (c) plasma temperature and (d) toroidal rotation frequency at different times during compression respectively. The dashed lines indicate the locations of $r = r_s$ for the corresponding times. The simulation is same as the case shown in figure 9(b).